Dynamical glass in weakly nonintegrable Klein-Gordon chains

Carlo Danieli,[1] Thudiyangal Mithun,[1] Yagmur Kati,[1,2] David K. Campbell,[3] and Sergej Flach[1,4]
[1]*Center for Theoretical Physics of Complex Systems, Institute for Basic Science, Daejeon 34126, Republic of Korea*
[2]*Basic Science Program, Korea University of Science and Technology (UST), Daejeon 34113, Republic of Korea*
[3]*Department of Physics, Boston University, Boston, Massachusetts 02215, USA*
[4]*New Zealand Institute for Advanced Study, Massey University, Auckland 02215, New Zealand*

(Received 27 November 2018; revised manuscript received 19 August 2019; published 25 September 2019)

Integrable many-body systems are characterized by a complete set of preserved actions. Close to an integrable limit, a *nonintegrable* perturbation creates a coupling network in action space which can be short or long ranged. We analyze the dynamics of observables which become the conserved actions in the integrable limit. We compute distributions of their finite time averages and obtain the ergodization time scale T_E on which these distributions converge to δ distributions. We relate T_E to the statistics of fluctuation times of the observables, which acquire fat-tailed distributions with standard deviations σ_τ^+ dominating the means μ_τ^+ and establish that $T_E \sim (\sigma_\tau^+)^2/\mu_\tau^+$. The Lyapunov time T_Λ (the inverse of the largest Lyapunov exponent) is then compared to the above time scales. We use a simple Klein-Gordon chain to emulate long- and short-range coupling networks by tuning its energy density. For long-range coupling networks $T_\Lambda \approx \sigma_\tau^+$, which indicates that the Lyapunov time sets the ergodization time, with chaos quickly diffusing through the coupling network. For short-range coupling networks we observe a *dynamical glass*, where T_E grows dramatically by many orders of magnitude and greatly exceeds the Lyapunov time, which satisfies $T_\Lambda \lesssim \mu_\tau^+$. This effect arises from the formation of highly fragmented inhomogeneous distributions of chaotic groups of actions, separated by growing volumes of nonchaotic regions. These structures persist up to the ergodization time T_E.

DOI: 10.1103/PhysRevE.100.032217

I. INTRODUCTION

Ergodicity and mixing are central concepts in statistical mechanics. Both properties characterize the temporal evolution of a dynamical system: ergodicity demands that a solution visits almost all states of the available phase space; mixing requires that, as the system evolves, any choice of two open sets of available states will eventually overlap [1]. With mixing being a necessary condition for ergodicity, both constitute fundamental aspects of the phenomenon of thermalization. In particular, both properties imply that the available phase space does not fragment into inaccessible open sets, and that the infinite time average of any observable matches its phase space average. The latter feature typically acts as a definition of ergodicity. The search for the violation of ergodicity, mixing, and thermalization gave rise to some of the most important discoveries in mathematics and statistical physics. Several of these results were found for *weakly nonintegrable systems*: models of N degrees of freedom whose Hamiltonians $H = H_0 + \bar{\varepsilon} H_1$ consist of an integrable part H_0, a nonintegrable perturbation H_1, and the perturbation strength $\bar{\varepsilon}$. In 1954 Kolmogorov proved the existence for small enough perturbation strength $0 < \bar{\varepsilon} < \bar{\varepsilon}_0$ of sets with nonzero measure of infinite time stable solutions which are confined to N-dimensional manifolds of the phase space (later labeled KAM tori) [2]. His work was extended by Arnold [3] and Moser [4] to larger classes of Hamiltonian systems, leading to the celebrated KAM theorem. Almost concomitantly with the discovery made by Kolmogorov, a numerical test on a small chain of harmonic oscillators in the presence of weak anharmonic coupling failed to show the expected equipartition of energy along the chain (original report in Ref. [5], reviews in Refs. [6–8]). This computer experiment, performed by Fermi, Pasta, Ulam and Tsingou (FPUT), and the attempts to explain its striking outcomes, led to the discovery of solitons [9,10] and to remarkable advances in the theory of Hamiltonian chaos [11–13]. In particular, it was found that a large number of weakly nonintegrable lattices possess families of exact time periodic solutions whose actions turn into the ones of the integrable system H_0 for $\varepsilon = 0$. Depending on the limit being considered, these solutions are called either (1) *discrete breathers* [14–17] and show typically exponential localization of energy in real space or (2) *q-breathers* which show exponential localization of energy in normal mode space [18,19]. Although forming a set of zero measure, these coherent solutions can impact the dynamical properties of a many-degrees-of-freedom system, since a generic trajectory can spend long times in their neighborhoods in phase space [20–26]. These events (also labeled *excursions out of equilibrium*) have been experimentally studied in the context of semiconductor lasers [27], superfluids [28], microwave cavities [29], optical fibers [30], and arrays of waveguides [31,32], among others.

The impact of these excursions on the ergodic properties has been studied in the past for spin glasses [33] and time-continuous random walks [34–37]. Recently an efficient numerical method to quantify the impact of the above excursions out of equilibrium in weakly nonintegrable Hamiltonian systems was proposed in Refs. [38,39]. That scheme chooses the actions at the integrable limit as the relevant observables and subsequently tracks their temporal fluctuations. The resulting distributions of fluctuation times and their finite time average distributions permit one to extract a novel ergodization time scale T_E [40]. The dependence of T_E on the strength of nonintegrable perturbation $\bar{\varepsilon}$, in particular its divergence for vanishing $\bar{\varepsilon}$, will signal the approaching of the integrable limit.

In this work we show that a nonintegrable perturbation H_1 can span different classes of interaction networks among the actions of the integrable limit H_0. These classes differ by network type being long range (respectively, short range). This distinction allows us to show that the Lyapunov time T_Λ—the inverse largest Lyapunov exponent—controls the ergodization dynamics and time scales for long-range networks, whereas it does not in the short-range case. We use a simple model—the Klein-Gordon (KG) chain for our computational studies. This model—as well as many other systems—exhibits all the above qualitatively different integrable limits. The paper is organized as follows. In the next section, we introduce weakly nonintegrable Hamiltonian systems and define long and short networks of actions. We then present our numerical studies of the different integrable limits of the Klein-Gordon chain. In the concluding section, we recap and discuss our results. A series of Appendixes provides technical details.

II. WEAKLY NONINTEGRABLE HAMILTONIAN SYSTEMS AND NETWORKS OF ACTIONS

Consider a Hamiltonian H with N degrees of freedom,

$$H = H(p, q), \tag{1}$$

where $q = (q_1, \dots, q_N)$ are the position coordinates and $p = (p_1, \dots, p_N)$ are the conjugate momenta. These coordinates belong to the $2N$-dimensional phase space $X = \mathbb{R}^N \times \mathbb{R}^N$. The equations of motion are

$$\dot{p}_n = -\frac{\partial H}{\partial q_n}, \quad \dot{q}_n = \frac{\partial H}{\partial p_n}. \tag{2}$$

An integral of motion I (e.g., the Hamiltonian energy H) is a quantity that is conserved along the solutions of Eqs. (2). The existence of ℓ integrals of motion implies that a trajectory is confined to a codimension ℓ submanifold, called the *available phase space*. A Hamiltonian H is called *integrable* if there exists a canonical transformation $(p, q) = \phi(J, \theta)$ that maps the conjugate coordinates (p, q) into action-angle coordinates (J, θ) such that

$$H(\phi(J, \theta)) \equiv H_0(J) \tag{3}$$

so that the Hamiltonian H_0 depends only on the actions $\{J_n\}_{n=1}^N$. The existence of such a canonical transformation ϕ is ensured by the Liouville-Arnold theorem [41]. The equations of motion (2) of an integrable system expressed in action-angle coordinates read

$$\dot{J}_n = -\frac{\partial H_0}{\partial \theta_n} = 0, \quad \dot{\theta}_n = \frac{\partial H_0}{\partial J_n} = \omega_n(J). \tag{4}$$

Solutions of Eqs. (4) yield constant actions $J_n(t)$ and time-periodic angles $\theta_n(t)$ that wind on N-dimensional tori $\mathbb{T}^N$:

$$J_n(t) = J_n^0, \quad \theta_n(t) = \omega_n t + \theta_n^0, \tag{5}$$

for the frequencies ω_n. Consequently, the phase space X is foliated by a set of invariant tori $\mathbb{T}^N$, where the solutions in Eqs. (5) are confined for all times $t \in \mathbb{R}$.

Let us consider a general Hamiltonian H and define the energy density $h = H/N$. If in regimes of small or large h some of its terms become negligible with respect to an otherwise integrable reminder H_0, we say that H possesses an *integrable limit*. This can be realized by considering a Hamiltonian of the form

$$H = H_0 + \bar{\varepsilon} H_1, \tag{6}$$

where H_0 is integrable, and H_1 is a nonintegrable perturbation whose strength is controlled by a small parameter $0 < \bar{\varepsilon} \ll 1$. Then Eqs. (2) read

$$\dot{\theta}_n = \omega_n(J) + \bar{\varepsilon} V_n(J, \theta), \quad \dot{J}_n = -\bar{\varepsilon} W_n(J, \theta), \tag{7}$$

where $V_n = \partial H_1/\partial J_n$ and $W_n = \partial H_1/\partial \theta_n$. We call the system in Eq. (6) weakly nonintegrable. For $\bar{\varepsilon} \neq 0$, the term W_n links the time dynamics of an action J_n to all or a subset of actions and angles of the system. In a typical case, each action J_n is connected to a number R_n of groups of actions, $\{G_m\}_{m=1}^{R_n}$, each one formed by $L_{n,m}$ actions $G_m = \{J_{g_{n,m}(l)}\}_{l=1}^{L_{n,m}}$. It then follows that a nonintegrable perturbation defines a network between the actions $\{J_n\}_{n=1}^N$, where R_n and $L_{n,m}$ depend on H_1. We henceforth distinguish networks according to how the number of groups of actions linked by the perturbation H_1 depends on the number of degrees of freedom, N. Let us define the *coupling range* $\mathcal{R} = \max\{R_n | n \leqslant N\}$. We can then distinguish the following two cases:

Long-range network (LRN). The coupling range $\mathcal{R}$ increases with the number N of degrees of freedom of the system, $\mathcal{R} = g(N)$, for a certain monotonic function g.

Short-range network (SRN). The coupling range $\mathcal{R}$ is finite and independent from the number N of degrees of freedom of the system.

III. THE MODEL

We consider a class of classical translation-invariant interacting many-body systems described by the Hamiltonian

$$H = \sum_{n=1}^{N} \left[\frac{p_n^2}{2} + V(q_n) + \varepsilon W(q_{n+1} - q_n) \right], \tag{8}$$

where V is a local potential and W is an interaction potential, with $V(0) = W(0) = V'(0) = W'(0) = 0$, $V''(0), W''(0) > 0$. We focus on the KG chain, for which

$$V(q) = \frac{q^2}{2} + \frac{q^4}{4}, \quad W(q) = \frac{q^2}{2}. \tag{9}$$

The equations of motion (2) read

$$\ddot{q}_n = -q_n - q_n^3 + \varepsilon(q_{n+1} + q_{n-1} - 2q_n). \tag{10}$$

Let us discuss several different integrable limits using ε and the energy density h as control parameters. For $h = \text{const}$, $\varepsilon \to 0$ and equally $h \to \infty$, $\varepsilon = \text{const}$ the system reaches an integrable set of decoupled oscillators, with the interaction potential W acting as the perturbation H_1 in Eq. (6), and the network is SRN. In contrast, $h \to 0$, $\varepsilon = \text{const}$ is a LRN integrable limit, since the quartic term in the local potential V becomes negligible with respect to the remaining quadratic ones. In this limit, the KG chain reduces to a chain of harmonic oscillators. The term $q_n^4/4$ (transformed to Fourier space) couples all the normal modes to each other and yields a long-range network. We note that the KG Hamiltonian possesses only one conserved quantity H. Equation (10) will be integrated in time using symplectic schemes (see Appendix A).

IV. METHODS

We follow the dynamics of time-dependent observables J which become conserved at the chosen integrable limit. *Ergodicity* away from the integrable limit would imply that their *infinite* time average equals their statistical average $\langle J\rangle$:

$$\lim_{T\to\infty}\overline{J}_T = \lim_{T\to\infty} = \frac{1}{T}\int_0^T J(t)dt = \langle J\rangle. \tag{11}$$

We numerically compute the finite time averages $\overline{J}_T$ for M different trajectories and obtain their distribution $\rho(\overline{J};T)$. This distribution is characterized by a first moment μ_J and a nonzero variance $\sigma_J^2(T)$. From Eq. (11) it follows that $\rho(\overline{J};T\to\infty)=\delta(\overline{J}-\langle J\rangle)$. We study this convergence by computing the dimensionless squared coefficient of variation (also called the fluctuation index):

$$q(T)=\frac{\sigma_J^2(T)}{\mu_J^2}. \tag{12}$$

Following Ref. [40], we extract an ergodization time scale T_E as

$$q(T)\sim\begin{cases} q(0) & \text{for } T\ll T_E\\ \frac{T_E}{T} & \text{for } T\gg T_E.\end{cases} \tag{13}$$

We further study the fluctuation statistics of $J(t)$ by computing the piercing times t^i at which $J(t)=\langle J\rangle$. The excursion times

$$\tau^{\pm}(i)=t^{i+1}-t^i \tag{14}$$

are distinguished between $J(t)>\langle J\rangle$ (τ^+) and $J(t)<\langle J\rangle$ (τ^-). We then compute numerically the distributions $P^{\pm}$ of the excursion times $\tau^{\pm}$, as well as their averages $\mu_\tau^{\pm}$ and their standard deviations $\sigma_\tau^{\pm}$ (see Appendix B for details). In particular, we focus on the τ^+ events (see Appendix C). These time scales dictate the ergodization time scales T_E according to Ref. [40],

$$T_E\sim\tau_q^+\equiv\frac{(\sigma_\tau^+)^2}{\mu_\tau^+}, \tag{15}$$

when neglecting correlations between different events (see Appendix E for details). Finally, we relate the ergodization time T_E to the Lyapunov time,

$$T_\Lambda = 1/\Lambda, \tag{16}$$

defined as the inverse of the largest Lyapunov exponent Λ and numerically obtained via the tangent method (see Appendix F for details). The dynamics of a nonintegrable system will be essentially identical to that of an integrable (but usually unknown) approximation precisely up to the time scale T_Λ.

V. LONG-RANGE NETWORK

Let us consider the small energy limit $h\to 0$, $\varepsilon=\text{const}$ of the KG chain. The integrable Hamiltonian H_0 consists of a chain of harmonic oscillators

$$H_0=\sum_{n=1}^{N}\left[\frac{p_n^2}{2}+\frac{q_n^2}{2}+\frac{\varepsilon}{2}(q_{n+1}-q_n)^2\right]. \tag{17}$$

The nonintegrable perturbation is then given by

$$\bar{\varepsilon}H_1=\sum_{n=1}^{N}\frac{q_n^4}{4}. \tag{18}$$

We choose fixed boundary conditions $p_0=p_{N+1}=q_0=q_{N+1}=0$, in analogy with the small energy limit of the Fermi-Pasta-Ulam (FPU) chain [5], in order to remove degeneracies of eigenmode frequencies.

We use the canonical transformation to normal mode momenta and coordinates $\{P_k,Q_k\}$

$$\begin{pmatrix}P_k\\Q_k\end{pmatrix}=\sqrt{\frac{2}{N+1}}\sum_{n=1}^{N}\begin{pmatrix}p_n\\q_n\end{pmatrix}\sin\left(\frac{\pi nk}{N+1}\right) \tag{19}$$

for $k=1,\dots,N$. This transformation diagonalizes the Hamiltonian $H_0=\sum_{k=1}^{N}E_k$ in Eq. (17), where the normal mode energies E_k are

$$E_k=\frac{P_k^2+\Omega_k^2Q_k^2}{2},\quad \omega_k=2\sin\left(\frac{\pi k}{2(N+1)}\right), \tag{20}$$

for $\Omega_k\equiv\sqrt{1+\varepsilon\omega_k^2}$. The equations of motion (10) in the normal mode coordinates [Eq. (19)] then read

$$\ddot{Q}_k+\Omega_k^2Q_k=-\frac{1}{2(N+1)}\sum_{l_1,l_2,l_3}A_{k,l_1,l_2,l_3}Q_{l_1}Q_{l_2}Q_{l_3}, \tag{21}$$

where

$$A_{k,l_1,l_2,l_3}=\delta_{k-l_1+l_2-l_3,0}+\delta_{k-l_1-l_2+l_3,0}-\delta_{k+l_1+l_2-l_3,0}-\delta_{k+l_1-l_2+l_3,0} \tag{22}$$

represents the coupling between the Fourier coordinates Q_k. Using the canonical transformation

$$Q_k=\sqrt{2J_k}\sin\theta_k,\quad P_k=\Omega_k\sqrt{2J_k}\cos\theta_k, \tag{23}$$

it follows that

$$\dot{J}_k=-\frac{1}{\Omega_k}\sum_{l_1,l_2,l_3}\mathscr{A}_{k,l_1,l_2,l_3}\sqrt{J_kJ_{l_1}J_{l_2}J_{l_3}}, \tag{24}$$

where the coefficients $\mathscr{A}_{k,l_1,l_2,l_3}$ depend on the angles $\{\theta_k\}_k$:

$$\mathscr{A}_{k,l_1,l_2,l_3}=\frac{A_{k,l_1,l_2,l_3}}{2(N+1)}\cos\theta_k\sin\theta_{l_1}\sin\theta_{l_2}\sin\theta_{l_3}. \tag{25}$$

For each action J_k, the sum on the right-hand side of Eq. (24) involves $R_k=N^2$ groups of variables $\{J_k\}$ due to the constrain enforced by Eq. (22). Each of the $m\leqslant R_k$ groups is formed by $L_{k,m}=4$ actions. Hence the coupling range $\mathcal{R}$—the integer which counts the number of connections $\mathcal{R}=\max\{R_k|k\leqslant N\}$—is $\mathcal{R}=N^2$, and this limit leads to a long-range network of actions J_k, similar to the FPU case discussed in Ref. [42].

We use the normal mode energies $E_k=\Omega_k^2J_k$ as the time-dependent observables, which are statistically distinguishable.

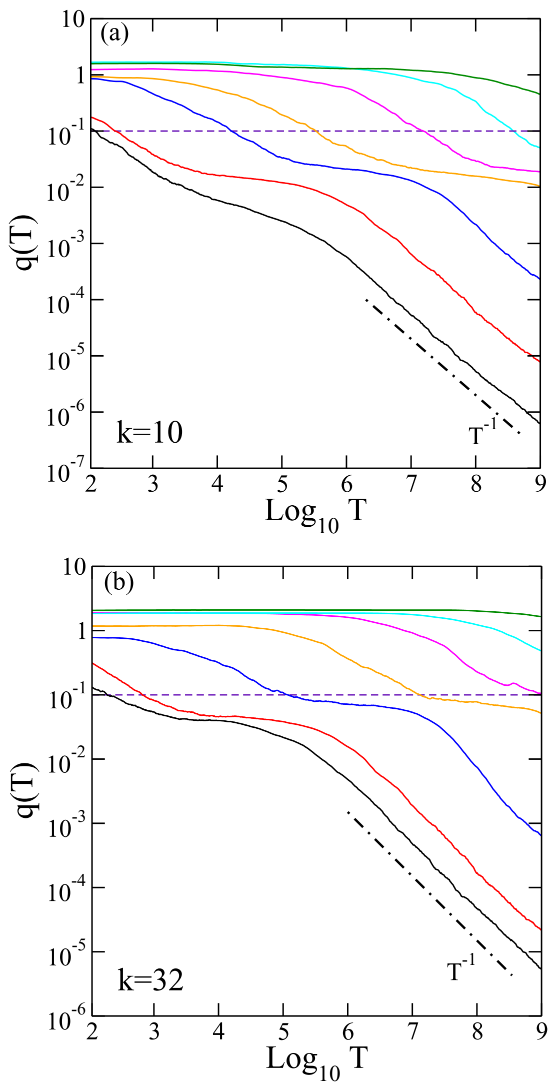

FIG. 1. (a) Squared coefficient of variation $q(T)$ computed for (top to bottom) $h = 0.0025$ (green), $h = 0.005$ (cyan), $h = 0.01$ (magenta), $h = 0.025$ (orange), $h = 0.1$ (blue), and $h = 1$ (red); $h = 3.5$ (black) obtained for mode $k = 10$. (b) Same as (a) for $k = 32$. The black dash-dotted lines guide the eye and indicate the algebraic decay. The violet dashed horizontal lines indicate the $q = 0.1$ threshold. Here $\varepsilon = 1$, $N = 2^5$, and $M = 2^9$.

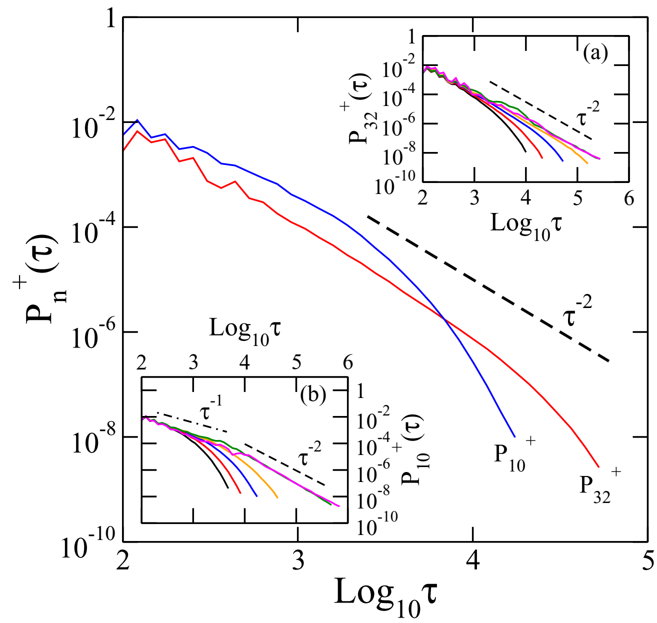

FIG. 2. $P^+_{10}(\tau)$ (blue) and $P^+_{32}(\tau)$ (orange) for $h = 0.05$. (a) $P^+_{32}(\tau)$ obtained for $h = 0.1$ (black), $h = 0.075$ (red), $h = 0.05$ (blue), $h = 0.03$ (orange), $h = 0.01$ (green), and $h = 0.005$ (magenta). (b) Same as (a) for $P_{10}(\tau)$. The dashed lines guide the eye and indicate the algebraic decay. Here $N = 2^5$, $\varepsilon = 1$, $M = 2^9$, and $T = 10^9$.

In Fig. 1, we show $q(T)$ for two different modes: one located in the band center $k = 10$ [Fig. 1(a)] and one in the band edge $k = 32$ [Fig. 1(b)] for different h fixing $\varepsilon = 1$ for a system of $N = 2^5$ oscillators and averaging over $M = 2^9$ initial conditions. In both cases, the asymptotic decay $q(T) \sim T_E/T$ is visible for the larger energy cases (from black to blue). We estimate T_E using $q(T_E) = 0.1$ (horizontal dashed lines in Fig. 1; see Appendix G for details). For $q = 0.1$ the distribution ρ shows substantial convergence to its limiting δ function profile, and varying the cutoff condition does not affect the outcome up to a common scaling prefactor (see Appendix H for examples).

In Fig. 2 we show the distributions for the $k = 32$ mode [P^+_{32} (red)] and the $k = 10$ mode [P^+_{10} (blue)] of the excursion times τ^+_k for $h = 0.05$ and $\varepsilon = 1$. These distributions differ from each other in accord with the statistical distinguishability of the actions. In Figs. 2(a) and 2(b) of we show P^+_{32} and P^+_{10}, respectively, for various values of h. Both cases show intermediate (though different) power-law tail trends; namely, P^+_{32} shows intermediate τ^{-2}, while P^+_{10} shows two consecutive intermediate power-law transient regions τ^{-1} and τ^{-2}, respectively. We extract and use in the following the averages $\mu^+_{\tau,k}$ and the standard deviations $\sigma^+_{\tau,k}$ of the excursion times τ^+.

In Fig. 3 we compare all computed time scales for mode number $k = 10$ [Fig. 3(a)] and $k = 32$ [Fig. 3(b)] as a function of h. We plot the measured T_E with orange squares, while we use red diamonds for averages $\mu^+_{\tau,10}$, $\mu^+_{\tau,32}$ and blue triangles for deviations $\sigma^+_{\tau,10}$, $\sigma^+_{\tau,32}$. We observe that $\sigma^+_{\tau,k} \approx \mu^+_{\tau,k}$ at $h = 1$. For $h \to 0$, $\sigma^+_{\tau,k} \gg \mu^+_{\tau,k}$ in accord with the above observed fat tails of the corresponding distribution functions P^+. We then plot $A\tau^+_{q,k}$ using green circles for a fitting parameter $A = 166$ (see Ref. [43] for details) and confirm the predicted relation between the excursion time statistics and the ergodization time T_E in Eq. (15). Finally we plot in Fig. 3 the Lyapunov time T_Λ (black stars). In both cases $k = 10$ and $k = 32$, $T_\Lambda \approx \sigma^+_{\tau,k}$, which indicates that the fat tails of the distributions of excursion times are controlled by the Lyapunov time. To illustrate this, we show T_E, $\mu^+_{\tau,k}$, $\sigma^+_{\tau,k}$, and $A\tau^+_{q,k}$ in units of T_Λ, and as a function of T_Λ in Figs. 3(c) and 3(d).

VI. SHORT-RANGE NETWORK

We use periodic boundary conditions $p_1 = p_{N+1}$, $q_1 = q_{N+1}$. In the limit of weak coupling $\varepsilon \ll 1$, $h = \text{const}$ (respectively, $h \gg 1$, $\varepsilon = \text{const}$) the system of equations (8) and (9) is close to an integrable limit with an integrable Hamiltonian

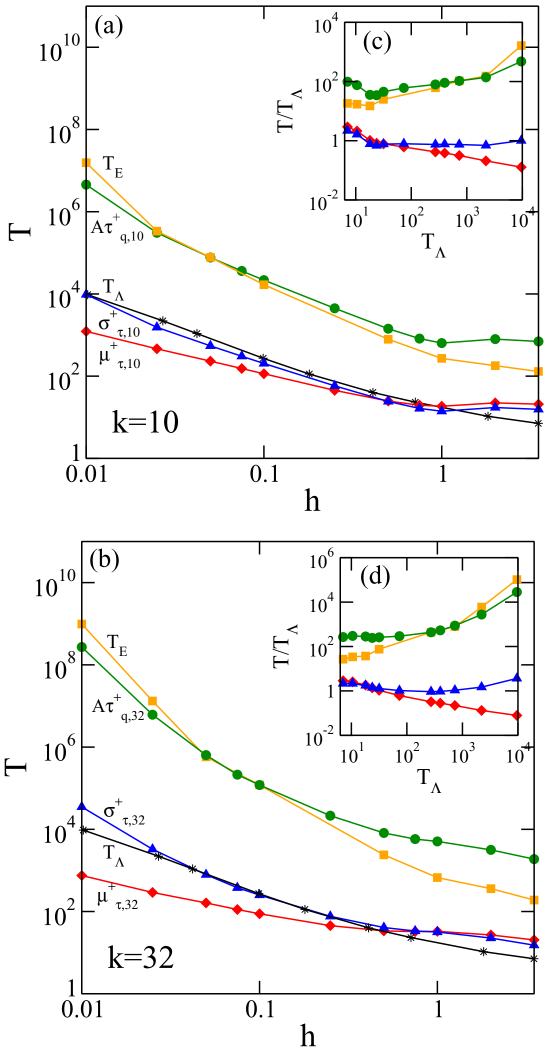

FIG. 3. (a) Time scales T_E (orange squares), $A\tau^+_{q,k}$ (green circles), $\sigma^+_{\tau,k}$ (blue triangles), $\mu^+_{\tau,k}$ (red diamonds), and T_Λ (black stars) vs the energy densities h for $k = 10$. (b) Same as (a) but for $k = 32$. (c) Rescaled times ($T_E, A\tau^+_{q,k}, \sigma^+_{\tau,k}, \mu^+_{\tau,k}$) in units of T_Λ. Here $N = 2^5$, $\varepsilon = 1$, $M = 2^9$, $A = 166$, and $T = 10^9$.

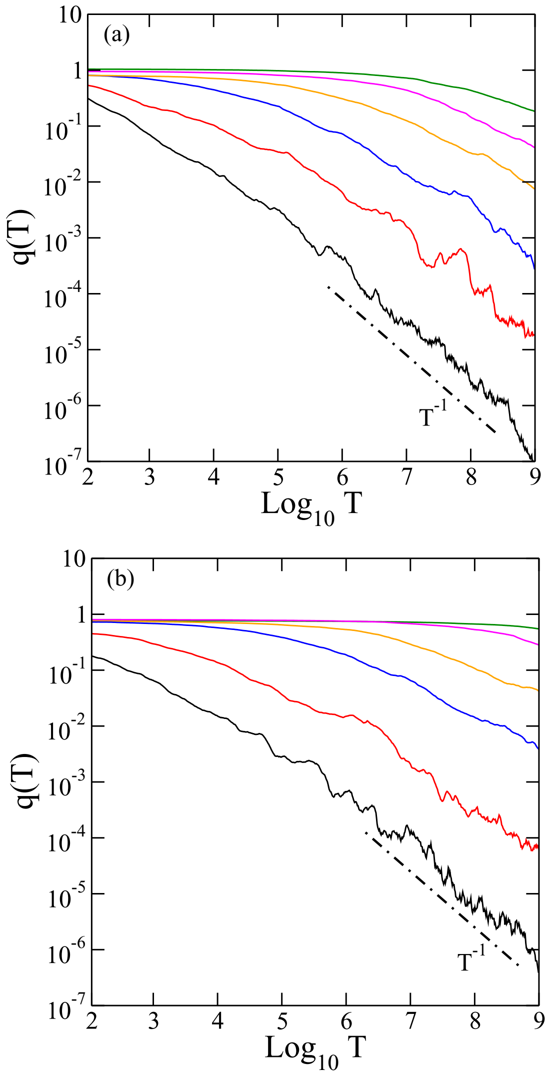

FIG. 4. (a) Squared coefficient of variation $q(T)$ computed for (top to bottom) $h = 12$ (green), $h = 6$ (magenta), $h = 3$ (orange), $h = 0.5$ (blue), $h = 0.1$ (red), and $h = 0.01$ (black) with $\varepsilon = 0.05$. (b) Same as (a) for (top to bottom) $\varepsilon = 0.015$ (green), $\varepsilon = 0.025$ (magenta), $\varepsilon = 0.05$ (orange), $\varepsilon = 0.1$ (blue), $\varepsilon = 0.3$ (red), and $\varepsilon = 0.8$ (black) with $h = 5$. The black dash-dotted lines guide the eye and indicate the algebraic decay. Here $N = 2^{10}$.

H_0 of a chain of decoupled anharmonic oscillators:

$$H_0 = \sum_{n=1}^{N} \left[\frac{p_n^2}{2} + \frac{q_n^2}{2} + \frac{q_n^4}{4} \right]. \qquad (26)$$

The nonintegrable perturbation is then given by

$$\bar{\varepsilon} H_1 = \frac{\varepsilon}{2} \sum_{n=1}^{N} (q_n - q_{n-1})^2. \qquad (27)$$

H_1 couples only nearest-neighboring oscillators, leading to a SRN of actions. As in Ref. [44], we choose

$$I_n = \frac{p_n^2}{2} + V(q_n) + \frac{\varepsilon}{4}[(q_{n+1} - q_n)^2 + (q_n - q_{n-1})^2] \qquad (28)$$

as the time-dependent observables, which become conserved in both integrable limits. Due to translation invariance, the observables I_n are statistically equivalent, fluctuating around the energy density h. Since their distributions of finite time averages and of fluctuation times are identical, we extract measurements from all sites and use them for the computation of the distributions (see Appendix I). That allows us to reduce the number of trajectories studied.

In Fig. 4 we show $q(T)$. Again $q(T) \sim q(0)$ for $T \ll T_E$, and $q(T) \sim T_E/T$ for $T \gg T_E$ in accord with Eq. (13). The ergodization time T_E is extracted by rescaling and fitting the curves (see Appendix G for details).

We compute the excursion times τ_n^+ of the observables I_n, and their distributions P^+. In Fig. 5 we show P^+ for different h with $\varepsilon = 0.05$ with $N = 2^8$. We notice that the distributions acquire fat fails, with an intermediate power-law trend τ^{-2} which extends as h grows. This is substantiated in the inset, where the local derivative $\gamma(\tau) \equiv d(\log_{10} P^+)/d(\log_{10} \tau)$ is shown. We also show in Fig. 5 the distributions P^+ computed

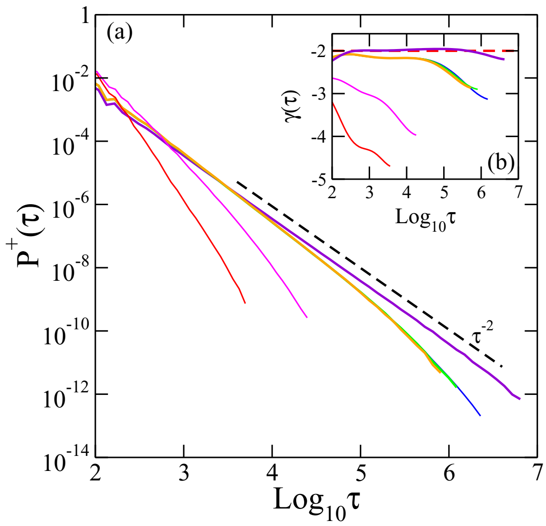

FIG. 5. (a) $P_+(\tau)$ obtained for (left to right) $h = 0.42$ (red), $h = 1.09$ (magenta), $h = 2.5$ (green), and $h = 5.31$ (violet) for $N = 2^8$. For $h = 2.5$, $P_+(\tau)$ is shown for $N = 2^7$ (orange) and $N = 2^{10}$ (blue) - see text for details. The dashed line guides the eye and indicates the algebraic decay. Inset (b): $\gamma(\tau) \equiv d(\log_{10} P^+)/d(\log_{10}\tau)$. Here $\varepsilon = 0.05$ and $T = 10^{10}$.

for a given $h = 2.5$ and $\varepsilon = 0.05$ and different system sizes $N = 2^7$, 2^8, and 2^{10} (orange, green, and blue curves) to confirm the absence of finite size corrections. We finally compute the average μ_τ^+ and the standard deviation σ_τ^+.

In Fig. 6 we compare all computed time scales for the large energy density regime $h \gg 1$, $\varepsilon = 0.05$ [Fig. 6(a)] and the weak-coupling regime $\varepsilon \ll 1$, $h = 5$ [Fig. 6(b)]. We found that T_E grows over several orders of magnitude. The standard deviation σ_τ^+ outgrows the average μ_τ^+ as the integrable limit is approached. We plot $A\tau_q^+$ for $A = 132$ (see Ref. [43] for details) and observe very good agreement with T_E.

Finally we compare T_E, μ_τ^+, σ_τ^+, and $A\tau_q^+$ with the Lyapunov time T_Λ (shown in black stars) as a function of h in Fig. 6(a) and ε in Fig. 6(b). In contrast to the long-range-network results where $T_\Lambda \approx \sigma_\tau^+$, in both short-range-network cases $T_\Lambda \lesssim \mu_\tau^+ \ll \sigma_\tau^+$. Consequently, $T_E \approx 10^9$ [at $h = 10$ for given $\varepsilon = 0.05$ in Fig. 6(a), and at $\varepsilon = 0.1$ for $h = 5$ in Fig. 6(b)] and $T_\Lambda \approx 10$, leaving a gap of eight orders of magnitude in time to be understood. In Fig. 6(c), we confirm the above statements by showing T_E, $\mu_{\tau,k}^+$, $\sigma_{\tau,k}^+$, and $A\tau_{q,k}^+$ in units of T_Λ, as a function of T_Λ. The observed widening temporal gap between T_Λ and T_E is similar to the short-range-network studies of a classical chain of Josephson junctions in Ref. [40] and signals the emergence of a dynamical glass [40].

VII. CONCLUSION

Our studies of the microcanonical dynamics of Klein-Gordon chains with up to 1024 degrees of freedom show that the distributions of finite time averages $\rho(\overline{J}_n; T)$ of integrable limit actions tend towards δ functions in the large-T limit. Consequently the extracted ergodization times T_E increase upon approaching the integrable limits but retain finite values at finite distance from the limits. We also computed the statistics of fluctuation times of $J_n(t)$. We found that both their average $\mu_{\tau,n}^+$ and standard deviation $\sigma_{\tau,n}^+$ diverge in the same integrable limits, as well as their dimensionless ratio $\sigma_{\tau,n}^+/\mu_{\tau,n}^+$ which indicates the emergence of fat tails. Assuming the statistical independence of fluctuation events, it follows that $(\sigma_{\tau,n}^+)^2/\mu_{\tau,n}^+ \sim T_E$ which was confirmed in all studied cases. Similar observations were obtained for classical chains of Josephson junctions [40], raising the interesting question of how general our findings are.

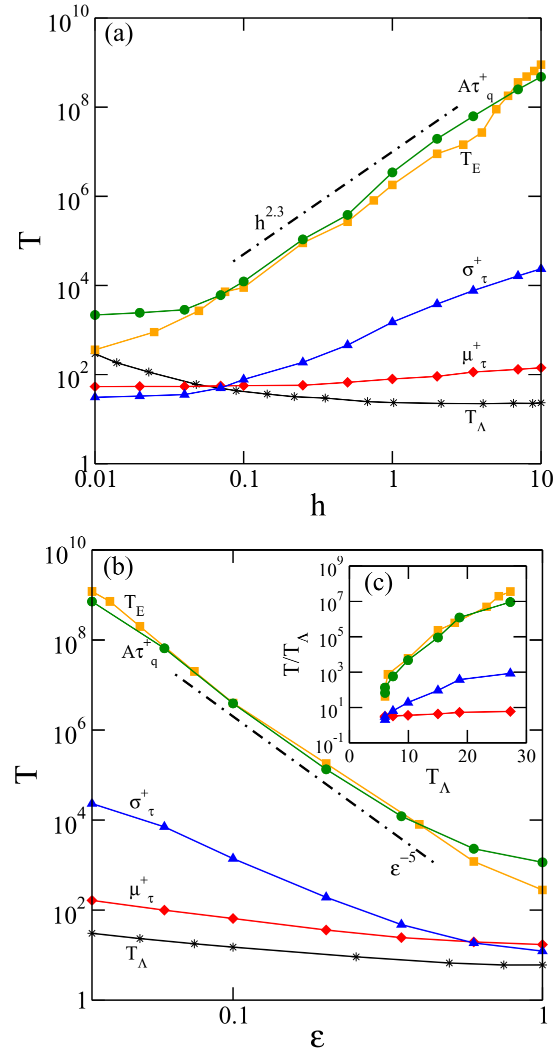

FIG. 6. (a) Time scales T_E (orange squares), $A\tau_q^+$ (green circles), σ_τ^+ (blue triangles), μ_τ^+ (red diamonds), and T_Λ (black stars) vs energy densities h for $\varepsilon = 0.05$. (b) Same as (a) but vs ε for $h = 5$. (c) Rescaled times (T_E, $A\tau_q^+$, σ_τ^+, μ_τ^+) in units of T_Λ. The black dash-dotted lines guide the eye. Here $N = 2^{10}$ and $A = 132$.

We studied two different types of integrable limits, characterized by long-range (respectively, short-range) networks between the actions J_n spanned by the nonintegrable perturbation. While the above findings appear to be generic for both cases, the comparison of the Lyapunov time T_Λ with the ergodization time scales shows remarkable differences between the two types of networks. For long-range networks, we find that $T_\Lambda \approx \sigma_{\tau,n}^+$ and consequently $T_E \sim T_\Lambda^2$. On the contrary, for short-range networks $T_\Lambda \approx \mu_{\tau,n}^+$ (see, e.g., Fig. 7). The latter observation is again in line with similar results obtained for

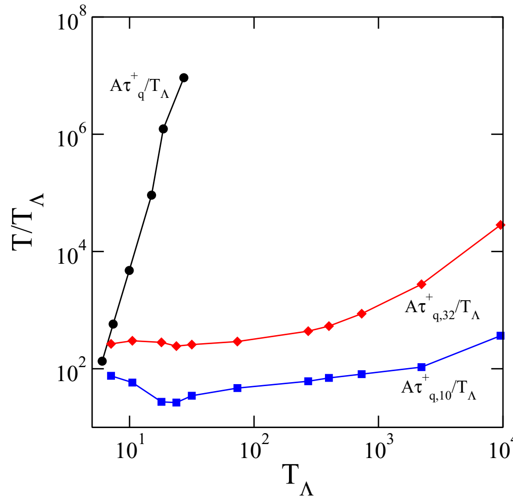

FIG. 7. $A\tau_q^+/T_\Lambda$ vs the Lyapunov time T_Λ for the anticontinuum limit (black circles) with $A = 132$, and the low-energy limit with $k = 32$ (red diamonds) and $k = 10$ (blue squares), both with $A = 166$.

classical chains of Josephson junctions [40], indicating the emergence of a dynamical glass.

Both types of networks are characterized by a finite coordination number L introduced in Sec. II. In the case of the KG model, this coordination number amounts to $L = 2$ for the SRN case and $L = 4$ for the LRN case. The Lyapunov time corresponds to the time scale on which the dynamics of resonant interacting multiplets of actions becomes chaotic, in accordance with Chirikov overlap criterion studies (see, e.g., Refs. [45–49]). Close to the corresponding integrable limit, the probability and corresponding density of resonant multiplets will diminish. In the case of a LRN, chaotic dynamics of any group of L resonant actions will still couple into the whole network. In contrast, in the case of SRN, the chaotic dynamics of a group of L resonant actions will couple only to its nearest neighbors, leaving the dynamics of the majority of all actions almost regular and unchanged. We conjecture that the rapidly widening gap between the ergodization time T_E and the Lyapunov time T_Λ for SRN is due to slow processes of diffusion, or meandering, or percolation, of resonance through the action network, as observed also for classical chains of Josephson junctions [40].

Many open questions remain. Among the most pressing ones are pushing the limits of our calculation to $N \to \infty$ of the SRN case where the finite size effects on $q(T)$ disappear. On the other hand, the considered large lattice for this case, $N = 1024$, hints that T_E remains the same even in the limit $N \to \infty$. Other challenges concern collecting evidence that the above observed scenarios of many-body Hamiltonian dynamics approaching integrable limits is generic, as well as the impact of quantization on the slow ergodization dynamics.

ACKNOWLEDGMENTS

The authors acknowledge financial support from the Institute for Basic Science (Project No. IBS-R024-D1). We thank I. Vakulchyk, A. Andreanov, M. Fistul, and Ch. Skokos for useful discussions.

APPENDIX A: NUMERICAL INTEGRATION

Our simulations were performed on the IBS-PCS cluster, which uses Intel E5-2680v3 processors. The time integrations were performed using a second order symplectic integrator $SABA_2C$ (see Ref. [50] for a general discussion on symplectic methods; see Ref. [51] for the explicit application of the integrator $SABA_2C$). The $SABA_2$ scheme consists in separating the Hamiltonian $H = A + B$, and approximates the resolvent $e^{\Delta t H}$ according to

$$\mathrm{SABA}_2 = e^{c_1 \Delta t L_A} e^{d_1 \Delta t L_B} e^{c_2 \Delta t L_A} e^{d_1 \Delta t L_B} e^{c_1 \Delta t L_A}, \tag{A1}$$

where $c_1 = \frac{1}{2}(1 - \frac{1}{\sqrt{3}})$, $c_2 = \frac{1}{\sqrt{3}}$, $d_1 = \frac{1}{2}$, and Δt is the time step. We split the Hamiltonian H in the KG system in Eq. (10) as

$$A = \sum_{n=1}^{N} \frac{p_n^2}{2}, \quad B = \sum_{n=1}^{N} \left[\frac{q_n^2}{2} + \frac{q_n^4}{4} + \frac{\varepsilon}{2}(q_{n+1} - q_n)^2 \right]. \tag{A2}$$

The resolvent operators $e^{\Delta t L_A}$ and $e^{\Delta t L_B}$ of the Hamiltonian A and B propagate the set of coordinates (q_n, p_n) at the time t to the final values (q_n', p_n') at the time $t + \Delta t$. These operators respectively read

$$e^{\Delta t L_A} : \begin{cases} q_n' = q_n + p_n \Delta t \\ p_n' = p_n, \end{cases} \tag{A3}$$

$$e^{\Delta t L_B} : \begin{cases} q_n' = q_n \\ p_n' = p_n + \{ -q_n(1 + q_n^2) \\ \qquad + \varepsilon(q_{n+1} + q_{n-1} - 2q_n)\}\Delta t. \end{cases} \tag{A4}$$

Following Ref. [51], we improve the accuracy of the $SABA_2$ scheme using a corrector $C = \{\{A, B\}, B\}$:

$$\mathrm{SABA}_2 C = e^{-\frac{g}{2}\Delta t^3 L_C} \mathrm{SABA}_2 e^{-\frac{g}{2}\Delta t^3 L_C} \tag{A5}$$

for $g = (2 - \sqrt{3})/24$. For the KG chain, the corrector C is

$$C = \sum_{n=1}^{N} \left[q_n(1 + q_n^2) + \varepsilon(2q_n - q_{n+1} - q_{n-1}) \right]^2. \tag{A6}$$

The corrector operator C yields the following resolvent operator:

$$e^{\Delta t L_C} : \begin{cases} q_n' = q_n \\ p_n' = p_n + 2\{[-q_n(1+q_n^2) + \varepsilon(q_{n+1} \\ \qquad + q_{n-1} - 2q_n)][1 + 3q_n^2 + 2\varepsilon] \\ \qquad + \varepsilon[q_{n-1}(1+q_{n-1}^2) - \varepsilon(q_n + q_{n-2} - 2q_{n-1})] \\ \qquad + \varepsilon[q_{n+1}(1+q_{n+1}^2) - \varepsilon(q_{n+2} + q_n - 2q_{n+1})]\}\Delta t. \end{cases} \tag{A7}$$

Note that for both resolvents $e^{\Delta t L_B}$ and $e^{\Delta t L_C}$ in Eqs. (A4) and (A7) the boundary conditions have to be applied: fixed boundary conditions for the LRN cases, and periodic boundary conditions for the SRN cases.

This scheme was implemented using a time step $\Delta t = 0.1$, keeping the relative energy error $\Delta E = |E(t) - E(0)|/E(0)$ of order 10^{-6}.

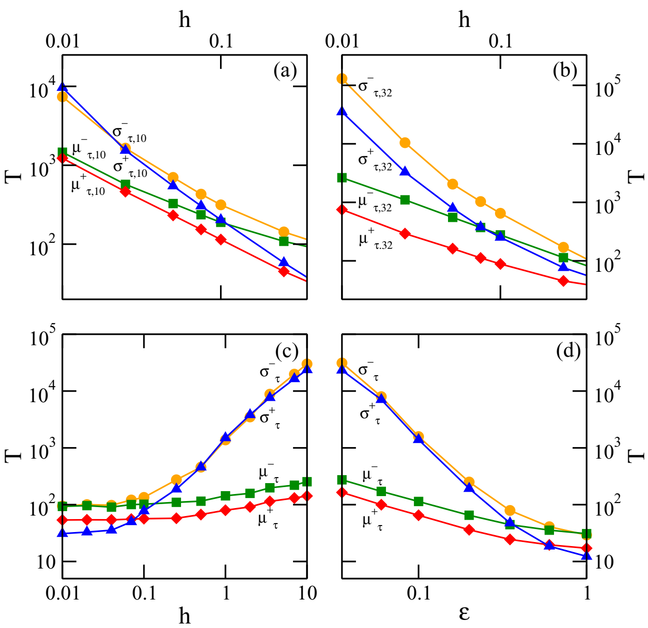

FIG. 8. (a) $\mu^+_{\tau,k}$ (red diamonds), $\mu^-_{\tau,k}$ (green squares), $\sigma^+_{\tau,k}$ (blue triangles), and $\sigma^-_{\tau,k}$ (orange circles) vs the energy density h for $k = 10$ and $\varepsilon = 1$. (b) Same as (a) for $k = 32$. In both (a) and (b), $M = 2^9$. (c) μ^+_τ (red diamonds), μ^-_τ (green squares), σ^+_τ (blue triangles), and σ^-_τ (orange circles) vs the energy density h for $\varepsilon = 0.05$. (d) Same as (c) vs ε for $h = 5$.

APPENDIX B: DISTRIBUTION P_k OF THE EXCURSION TIMES

In the numerical calculations of the PDF P_k of excursions out of equilibrium τ, we consider the interval $\mathcal{I}_b = [10^2, 10^b]$ to which the excursion times belong, and we separate this into M bins of logarithmic width [52]. Hence, the bins B_s are defined as

$$\mathcal{I}_b = \cup_{s=1}^{M} \mathcal{B}_s = \cup_{s=1}^{M} [10^{2+\kappa(s-1)}, 10^{2+\kappa s}] \qquad \text{(B1)}$$

with $\kappa = (b-2)/M$. From our plots, we exclude all the bins that count less than 100 events, as these should be considered as statistically not relevant. If one reduces this number, then the range of the tail of the computed distribution increases; however, it is at the expense of less statistical significance, and thus with strongly fluctuating tails. The smoothness of the tails is by itself enough evidence for the statistical significance of our data, and the chosen cutoff at 100 events ensures a numerical error of less than 10%. Let us remark that this cutoff is applied only to the numerical reconstruction of the distributions, but not to the calculation of the first moment $\mu^\pm_\tau$ and the standard deviation $\sigma^\pm_\tau$, where instead all detected events are included.

APPENDIX C: AVERAGE AND STANDARD DEVIATION OF $\tau^\pm_n$

In Fig. 8 we show the averages and the standard deviations of both τ^+_k and τ^-_k. The four plots [Figs. 8(a)–8(d)] correspond to the four cases discussed numerically in the main text, namely, $\mu^\pm_{\tau,k}$ and $\sigma^\pm_{\tau,k}$ for the low-energy regime with $k = 10$ [Fig. 8(a)] and for $k = 32$ [Fig. 8(b)], corresponding to Figs. 3(a) and 3(b), respectively; and $\mu^\pm_\tau$ and $\sigma^\pm_\tau$ for the large-energy limit [Fig. 8(c)] and anticontinuum limit [Fig. 8(d)] corresponding to Figs. 6(a) and 6(b), respectively. In all these cases, we observe that the average μ^+_τ of τ^+ (red diamonds) shows a divergence trend similar to μ^-_τ of τ^- (green squares). Similarly, the standard deviation σ^+_τ of τ^+ (blue triangles) shows a divergence trend like that of σ^-_τ of τ^- (orange circles). We then focus on the "+" events only, τ^+, which we recall are events during which $J_n > \langle J_n\rangle_X$.

APPENDIX D: ENSEMBLE OF INITIAL CONDITIONS

Let us assume that there exists only one conserved quantity of the system (the total energy H). We define the initial condition at $t = 0$ as zeroing the position coordinates $q_n = 0$ and distributing the half squares of kinetic energy $p_n^2/2$, according to the following distribution P_1 defined for a positive real number $C > 0$:

$$P_1(z) = Ce^{-Cz}, \quad z \in [0, \infty]. \qquad \text{(D1)}$$

From this, for a uniform distribution of random numbers $w(r)$ distributed in the range [0,1], one can get $z = -\log(w(r))/C$. This leads to a set of initial momenta coordinates $p_n^{(1)}$ at $t = 0$, where the sign is a discrete random variable, $a_n = \pm 1$ with distribution $P_2(a_n = \pm 1) = 0.5$. Here

$$p_n^{(1)} = a_n\sqrt{2z}. \qquad \text{(D2)}$$

The total energy E_T of the system is

$$E_T = \sum_{n=1}^{N} \frac{\left(p_n^{(1)}\right)^2}{2}. \qquad \text{(D3)}$$

We then set a chosen energy density h by the following rescaling:

$$p_n^{(2)} = \sqrt{\frac{hN}{E_T}}\, p_n^{(1)}. \qquad \text{(D4)}$$

The resulting momentum coordinates $p_n^{(2)}$ with the position coordinates $q_n = 0$ fixed at zero are evolved in time for $T_{IC} = 10^5$ using the SABA$_2C$ integrator with time step $\tau = 10^{-2}$, which keeps the relative energy error at $\Delta E \sim 10^{-9}$. We choose $T_{IC} = 10^5$ since it exceeds by one order of magnitude the largest Lyapunov time T_Λ we observed ($T_\Lambda \approx 10^4$, observed in Fig. 3 for $h = 0.01$ and $\varepsilon = 1$). No qualitative differences in the resulting measured time scales were noticed if larger prerun times T_{IC} were chosen. The result of this time evolution is then taken as an initial condition of our simulation. Then, M draws of the distributions P_1 and P_2 yield an ensemble of M initial conditions.

APPENDIX E: ASYMPTOTIC BEHAVIOR OF $q(T)$

In Eq. (15) we indicated that the ergodization time T_E of an observable J_n is proportional to the ratio between the variance $(\sigma^+_\tau)^2$ and the average μ^+_τ of its excursions out of equilibrium:

$$T_E \sim \tau^+_q \equiv \frac{(\sigma^+_\tau)^2}{\mu^+_\tau}. \qquad \text{(E1)}$$

We here derive this relation, which is based on the approximation of the time evolution of J_n with telegraphic random signal

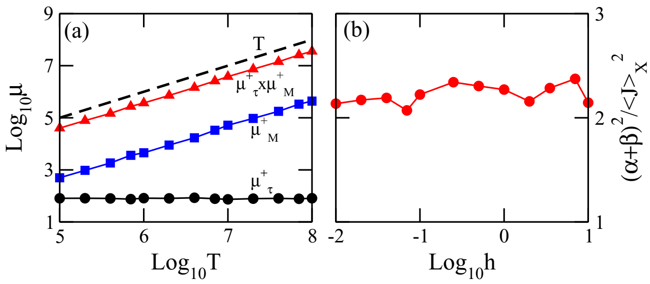

FIG. 9. (a) μ_τ^+ (black circles), μ_M^+ (blue squares), and their product $\mu_\tau^+ \times \mu_M^+$ (red), vs the integration time T obtained for $h = 5$ and $\varepsilon = 0.05$. The dashed line guides the eye and indicates the linear growth T. (b) $(\alpha+\beta)^2/\langle J\rangle_X^2$ vs the energy density h for $\varepsilon = 0.05$. Here $N = 2^{10}$.

[53–55]. Away from the integrable limit, an action J_n becomes a time-dependent variable $J_n(t) = \langle J_n\rangle_X + \phi_n(t)$, where ϕ_n is a continuous function fluctuating around zero. At the piercing times t_n^i of the action J_n, it follows that $\phi_n(t_n^i) = 0$. Then, the time average of J_n, here indicated as $B_n(T)$, is

$$B_n(T) = \frac{1}{T}\int_0^T J_n(t)dt = \langle J_n\rangle_X + \frac{1}{T}\int_0^T \phi_n(t)dt \equiv \langle J_n\rangle_X + D_n(T). \tag{E2}$$

The interval $[0, T]$ consists in M_n^+ events τ_n^+ and M_n^- of τ_n^-, plus uncompleted initial and final events of duration $\mathcal{I}_n$ and $\mathcal{E}_n$, respectively [56]. Let us observe that both $\mathcal{I}_n$ and $\mathcal{E}_n$ are not distributed according to the distribution $P_n^\pm$ of excursion times $\tau_n^\pm$. Nevertheless, for large values of M_n^+ and M_n^- we neglect their contribution. Hence, for all k it holds that

$$T = \sum_{i=1}^{M_n^+}\tau_n^+(i) + \sum_{i=1}^{M_n^-}\tau_n^-(i). \tag{E3}$$

The numbers $M_n^\pm$ of events $\tau_n^\pm$ are distributed according to the distributions $\rho_{M_n}^\pm$ and have an average $\mu_{M_n}^\pm$. In Fig. 9(a), we show that the average $\mu_{M_n}^+$ of the τ_n^+ scales typically as $\mu_{M_n}^+ \sim T/\mu_{\tau_n}^+$ as $T\to\infty$, where $\mu_{\tau_n}^+$ is the average of τ_n^+ computed for the short-range case of the KG chain using the observables J_n in Eq. (28). From Eq. (E3), we can write the integral over the interval $[0, T]$ in Eq. (E2) as a sum of integrals over the excursion times

$$\int_0^T \phi_n(t)dt = \sum_{i=1}^{M_n^+}\int_{t_n^i}^{t_n^{i+1}}\varphi_n^+(t)dt - \sum_{i=1}^{M_n^-}\int_{t_n^{i+1}}^{t_n^{i+2}}\varphi_n^-(t)dt \equiv \alpha_n\sum_{i=1}^{M_n^+}\tau_n^+(i) - \beta_n\sum_{i=1}^{M_k^-}\tau_n^-(i), \tag{E4}$$

where α_n and β_n are defined as

$$\alpha_n = \frac{\sum_{i=1}^{M_n^+}\int_{t_n^i}^{t_n^{i+1}}\varphi_n^+(t)dt}{\sum_{i=1}^{M_n^+}\tau_n^+(i)}, \quad \beta_k = \frac{\sum_{i=1}^{M_n^-}\int_{t_n^i}^{t_n^{i+1}}\varphi_n^-(t)dt}{\sum_{i=1}^{M_n^-}\tau_{n_n}^-(i)}. \tag{E5}$$

These coefficients α_n and β_n are distributed by the distributions ρ_{α_n} and ρ_{β_n}, respectively. Let us here define their averages α and β. We then approximate Eq. (E4) by the telegraphic noise signal

$$\int_0^T \phi_n(t)dt \approx \alpha\sum_{i=1}^{M_n^+}\tau_n^+(i) - \beta\sum_{i=1}^{M_n^-}\tau_{n_n}^-(i) \equiv \alpha S_n^+ - \beta S_n^-. \tag{E6}$$

Let us now consider the limit of $q(T)$ for $T\to\infty$. Due to the continuity of ϕ_n and the finiteness of all moments of the excursion times $\tau_n^\pm$, the term $D_n(T)$ in Eq. (E2) converges to zero as $T\to\infty$. Then, it follows that $\lim_{T\to\infty}\mu_{J_n}^2(T) = \langle J_n\rangle_X^2$. Hence, supposing $\langle J_n\rangle_X \neq 0$, the limit of the index q is

$$\lim_{T\to\infty} q(T) = \lim_{T\to\infty}\frac{1}{\mu_{J_n}^2(T)}\lim_{T\to\infty}\sigma_{J_n}^2(T) = \frac{1}{\langle J_n\rangle_X^2}\lim_{T\to\infty}\sigma_{J_n}^2(T). \tag{E7}$$

Recalling the following properties of the variance for a constant A,

$$\sigma_{AJ_n}^2 = A^2\sigma_{J_n}^2, \quad \sigma_{A+J_n}^2 = \sigma_{J_n}^2, \tag{E8}$$

from Eq. (E2) it follows that

$$\sigma_{B_n(T)}^2 = \sigma_{D_n(T)}^2. \tag{E9}$$

We can restrict to the τ_n^+ events only in Eq. (E6) by adding and subtracting βS_n^+. It follows that

$$D_n(T) = \frac{1}{T}\int_0^T \phi_n(t)dt = \frac{1}{T}[\alpha S_n^+ - \beta S_n^-(\pm\beta S_n^+)] = \frac{1}{T}[(\alpha+\beta)S_n^+ - \beta(S_n^- + S_n^+)] = \frac{1}{T}[(\alpha+\beta)S_n^+ - \beta T] = \frac{\alpha+\beta}{T}S_n^+ - \beta. \tag{E10}$$

By Eq. (E8), the variance of B_n is

$$\sigma_{B_n(T)}^2 = \frac{(\alpha+\beta)^2}{T^2}\sigma_{S_n^+}^2. \tag{E11}$$

The excursion times τ_n^+ are identically distributed variables. Assuming these to be independent events, the variance $\sigma_{S_n^+}^2$ of the sum of the head events S_n^+ in Eq. (E10) is the product of the variance $(\sigma_{\tau,n}^+)^2$ of the head events multiplied by the number of events, M_n^+:

$$S_n^+ \equiv \sum_{i=1}^{M_n^+}\tau_n^+(i) \quad\Rightarrow\quad \sigma_{S_n^+}^2 = M_n^+(\sigma_{\tau,n}^+)^2. \tag{E12}$$

For $T \gg \mu_{\tau,n}^+$, we expect that $\mu_{M_n}^+ \sim T/\mu_{\tau,n}^+$. In Fig. 9(a) we report the averages μ_M^+ and μ_τ^+ of the number M_n^+ and the duration $\tau_n^+(i)$ of the events detected by all the observables J_n in Eq. (28) for $h = 5$ and $\varepsilon = 0.05$. This plot confirms the above expectation.

In Eq. (E12) we approximate the variable M_n^+ by its average $\mu_{M_n}^+$, which leads to

$$\sigma_{B_n(T)}^2 \sim (\alpha+\beta)^2\frac{(\sigma_{\tau,n}^+)^2}{\mu_{\tau,n}^+}\frac{1}{T}. \tag{E13}$$

Ultimately, this results in the formula

$$q(T) \sim \frac{(\alpha+\beta)^2}{\langle J_n\rangle_X^2}\frac{(\sigma_{\tau,n}^+)^2}{\mu_{\tau,n}^+}\frac{1}{T}. \tag{E14}$$

In Fig. 9(b) we show the energy density h dependence of the ratio $(\alpha+\beta)^2/\langle J_n\rangle_X^2$ introduced in Eq. (E14) computed for the short-range case of the KG chain using the observables J_n in Eq. (28) for $\varepsilon = 0.05$. Over three orders of magnitude, the ratio $(\alpha+\beta)^2/\langle J_n\rangle_X^2$ fluctuates between 2 and 2.5. Hence this ratio in Eq. (E14) does not contribute to the asymptotic trend of the fluctuation parameter $q(T)$ as the system approaches an integrable limit. It therefore follows that the time scale $(\sigma_{\tau,n}^+)^2/\mu_{\tau,n}^+$ is proportional to the ergodization time T_E defined in Eq. (13), as stated in Eq. (15).

APPENDIX F: LARGEST LYAPUNOV EXPONENT Λ

We compute the largest Lyapunov exponent Λ by considering a small amplitude deviation vector $w(t) = (\delta q(t), \delta p(t))$ of a trajectory. We then numerically solve the variational equations

$$\dot{w}(t) = \left[J_{2N}\cdot D_H^2(x(t))\right]\cdot w(t) \tag{F1}$$

associated with a Hamiltonian H using the tangent method [57–59], where D_H^2 is the Hessian matrix and J_{2N} the symplectic matrix. Solving Eq. (F1) using the SABA$_2C$ integration scheme presented in Appendix A yields extended resolvent operators $e^{\Delta t L_A}$, $e^{\Delta t L_B}$, and $e^{\Delta t L_C}$ in Eqs. (A3), (A4), and (A7), where $(\delta q_n, \delta p_n)$ at the time t are simultaneously integrated to $(\delta q_n', \delta p_n')$ at the time $t+\Delta t$. The additional equations for $e^{\Delta t L_A}$ are

$$e^{\Delta t L_{AV}} : \begin{cases} \delta q_n' &= \delta q_n + \delta p_n \Delta t \\ \delta p_n' &= \delta p_n, \end{cases} \tag{F2}$$

while for $e^{\Delta t L_B}$ they are

$$e^{\Delta t L_{BV}} : \begin{cases} \delta q_n' &= \delta q_n + \delta p_n \Delta t \\ \delta p_n' &= \delta p_n + \left\{\varepsilon(\delta q_{n+1} + \delta q_{n-1}) \right. \\ & \quad \left. - \left[1 + 3q_n^2 + 2\varepsilon\right]\delta q_n\right\}\Delta t. \end{cases} \tag{F3}$$

For the correction term, we get

$$e^{\Delta t L_{CV}} : \begin{cases} \delta q_n' &= \delta q_n \\ \delta p_n' &= \delta p_n + \{\gamma_n \delta q_n + \gamma_{n+1}\delta q_{n+1}\gamma_{n+2}\delta q_{n+2} \\ & \quad + \gamma_{n-1}\delta q_{n-1} + \gamma_{n-2}\delta q_{n-2}\}\Delta t, \end{cases} \tag{F4}$$

where

$$\begin{aligned} \gamma_n &= -2\left\{\left[1+3q_n^2+2\varepsilon\right]^2 + 6q_n\left[q_n\left(1+q_n^2\right)\right.\right. \\ &\quad \left.\left. + \varepsilon(2q_n - q_{n+1} - q_{n-1})\right] + 2\varepsilon^2\right\}, \\ \gamma_{n+1} &= 2\varepsilon\left[2 + 4\varepsilon + 3q_n^2 + 3q_{n+1}^2\right], \\ \gamma_{n-1} &= 2\varepsilon\left[2 + 4\varepsilon + 3q_n^2 + 3q_{n-1}^2\right], \\ \gamma_{n+2} &= -2\varepsilon^2, \\ \gamma_{n-2} &= -2\varepsilon^2. \end{aligned} \tag{F5}$$

As mentioned above, in both resolvents $e^{\Delta t L_{BV}}$ and $e^{\Delta t L_{CV}}$ in Eqs. (F3) and (F4) the boundary conditions have to be applied: fixed boundary conditions for the LRN cases, and periodic boundary conditions for the SRN cases. The largest Lyapunov exponent Λ is computed by considering the limit

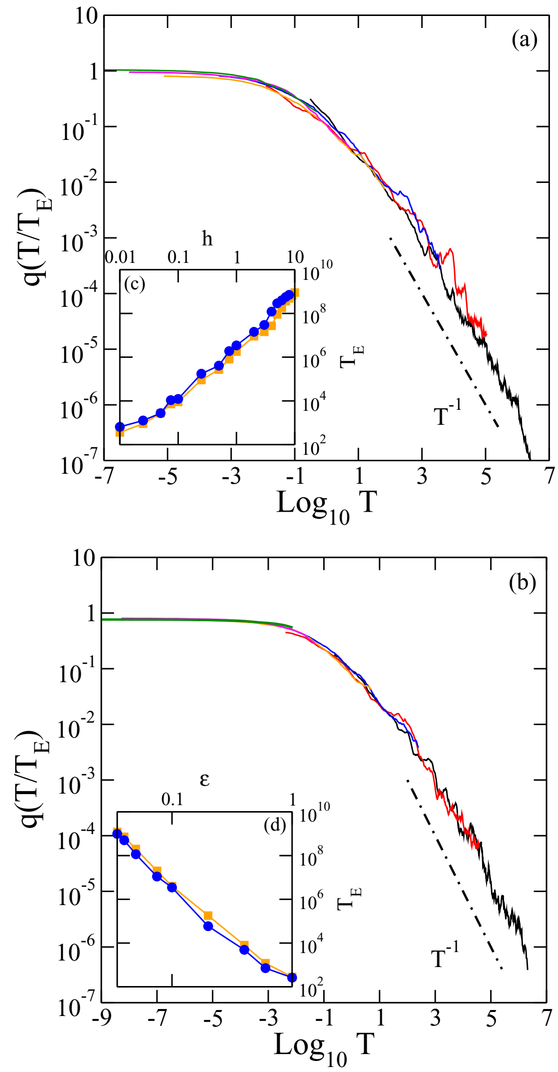

FIG. 10. (a) $q(T/T_E)$ vs T for the energy densities $h = 12$ (green), $h = 6$ (magenta), $h = 3$ (orange), $h = 0.5$ (blue), $h = 0.1$ (red), and $h = 0.01$ (black) with $\varepsilon = 0.05$. (c) See text for details. (b) Same as (a) vs the coupling strength $\varepsilon = 0.8$ (black), $\varepsilon = 0.3$ (red), $\varepsilon = 0.1$ (blue), $\varepsilon = 0.05$ (orange), $\varepsilon = 0.025$ (magenta), $\varepsilon = 0.015$ (green) with $h = 5$. Inset (d): see text for details. The dash-dotted lines guide the eye and indicate an algebraic trend. Here $N = 2^{10}$.

$$\Lambda = \lim_{t\to\infty}\frac{1}{t}\ln\frac{\|w(t)\|}{\|w(0)\|}, \tag{F6}$$

where $\|\cdot\|$ is a norm of the vector w. An extended presentation of this method applied to the KG chain can be found in Ref. [60].

APPENDIX G: MEASUREMENT OF THE COEFFICIENT T_E

In both Figs. 3 and 6 we have shown the behavior of the ergodization time T_E as the system approaches the integrable limit. In the cases shown in Fig. 6, T_E was determined by first extracting the prefactor of the power-law regression of

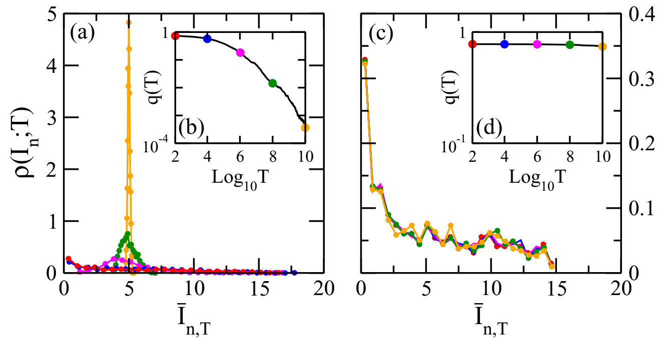

FIG. 11. (a) $\rho(I_n;T)$ for $\varepsilon = 0.1$ and different times $T = 10^2$ (red), $T = 10^4$ (blue), $T = 10^6$ (magenta), $T = 10^8$ (green), and $T = 10^{10}$ (orange) marked in (b), which reports the squared coefficient of variation $q(T)$. (c, d) Same as (a) and (b) for $\varepsilon = 0.005$. Here $h = 5$, $N = 2^{10}$.

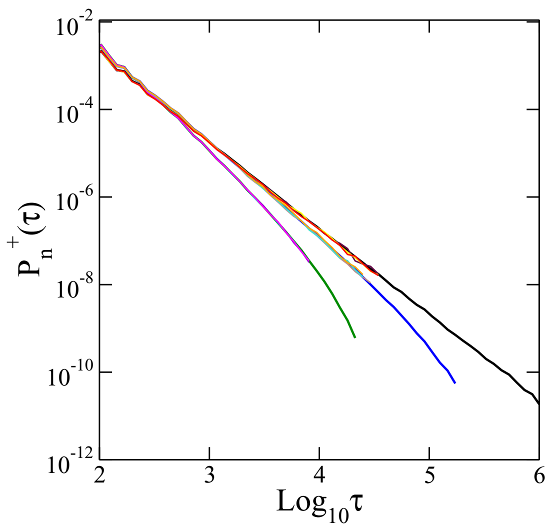

FIG. 12. $P_n^+(\tau)$ obtained for $\varepsilon = 1.01$ with $n = 1$ (cyan), $n = 16$ (violet), $n = 32$ (magenta), and all the I_n combined (green); for $\varepsilon = 2.88$ with $n = 1$ (brown), $n = 16$ (orange), $n = 32$ (turquoise), and all the I_n combined (blue); and for $\varepsilon = 12.9$ with $n = 1$ (red), $n = 16$ (maroon), $n = 32$ (yellow), and all the I_n combined (black). Here the system size is $N = 2^8$ and the total integration time is $T = 10^9$.

the black curve of both plots [corresponding to $h = 0.01$ in Fig. 4(a) and to $\varepsilon = 0.8$ in Fig. 4(b)]. We fix these as the two basic cases. Then, for all the higher h or lower ε cases, respectively, we rescaled the integration time $T \to T/x$ of the curve q by a factor x, and selected the proper $\hat{x}$ for which the rescaled curves align with their corresponding basic cases. The ergodization time T_E of each curve is finally obtained by multiplying its selected $\hat{x}$ with the ergodization time T_E of the corresponding basic case. In Fig. 10 we present the time evolution of the parameter q shown in Fig. 6 rescaled by the ergodization time T_E, to show the alignment between the curves. In the cases shown in Fig. 3, the intermediate plateau exhibited by the time evolution of the index q prevented us from obtaining a proper $1/T$ fitting and the rescaling of the integration time T using the techniques described above. Then, the ergodization time T_E was determined by the introduction of a cutoff at $q = 10^{-1}$ (violet dashed horizontal line in Fig. 1). We then test the reliability of this cutoff procedure on two SRN cases. In Fig. 10 we show the ergodization time T_E extracted by rescaling (orange squares) and by cutoff at $q = 10^{-1}$ (blue squares). The two sets of measurements show good agreement. We do not find significant changes in the scaling on T_E if different cutoff values are used (e.g., the value 0.075).

APPENDIX H: DISTRIBUTION ρ OF THE FINITE TIME AVERAGE

We here show the time dependence of the distribution ρ, corresponding to two cases of the weak coupling $\varepsilon \ll 1$, $h =$ const of the KG chain. Figure 11(a) is obtained for $\varepsilon = 0.1$, while Fig. 11(b) is instead obtained for $\varepsilon = 0.005$, both with $h = 5$. These plots show that the decay of the squared coefficient of variation q signals the convergence of the distribution ρ towards a δ function.

APPENDIX I: DISTRIBUTIONS P_n^+ IN THE SRN CASE

In Fig. 5 we plot the distribution function P^+ of the events τ^+ obtained by combining the events detected by all the observables J_n in Eq. (28) in one unique distribution. In Fig. 12 we show the distribution P_n^+ computed for the observables I_1, I_{16}, I_{32} and the distribution P^+ for all n combined for three different energies $h = 1.01$ (green), $h = 2.88$ (blue), and $h = 12.9$ (black). In the three cases, the distributions P_n^+ obtained with a single observable I_n overlap with each other and with the distribution P^+ obtained by combining the events detected by all I_n. The curves cannot be distinguished. This suggests that, due to translation invariance, the excursions out of equilibrium of each action I_n in Eq. (28) at a given distance from an integrable limit are governed by the same distribution.

[1] A. J. Lichtenberg and M. A. Lieberman, Regular and chaotic dynamics, in *Applied Mathematical Sciences* (Springer-Verlag, New York, 1992), Vol. 38.
[2] A. N. Kolmogorov, On conservation of conditionally periodic motions for a small change in Hamilton's function, Dokl. Akad. Nauk. SSSR 98, 527 (1954) [Engl. transl.: *Stochastic Behavior in Classical and Quantum Hamiltonian Systems*, Lecture Notes in Physics, 93, 51 (Springer, Como, 1979)].
[3] V. Arnold, A proof of a theorem by A. N. Kolmogorov on the invariance of quasi-periodic motions under small perturbations of the Hamiltonian, Russ. Math. Surv. **18**, 9 (1963).
[4] J. Moser, On invariant curves of area-preserving mappings of an annulus, Nachr. Akad. Wiss. Göttingen **1**, 1 (1962).
[5] E. Fermi, J. Pasta, and S. Ulam, in *Collected Papers of Enrico Fermi*, edited by E. Segré (University of Chicago Press, Chicago, 1965), Vol. 2, p. 978.

[6] J. Ford, The Fermi-Pasta-Ulam problem: Paradox turns discovery, Phys. Rep. **213**, 271 (1992).

[7] G. Gallavotti, *The Fermi-Pasta-Ulam Problem: A Status Report* (Springer, New York, 2008).

[8] M. A. Porter, N. J. Zabusky, B. Hu, and D. K. Campbell, Fermi, Pasta, Ulam and the birth of experimental mathematics, Am. Sci. **97**, 214 (2009).

[9] N. J. Zabusky and M. D. Kruskal, Interaction of "Solitons" in a Collisionless Plasma and the Recurrence of Initial States, Phys. Rev. Lett. **15**, 240 (1965).

[10] N. J. Zabusky and G. S. Deem, Dynamics of nonlinear lattices I. Localized optical excitations, acoustic radiation, and strong nonlinear behavior, J. Comput. Phys. **2**, 126 (1967).

[11] F. V. Izrailev and B. V. Chirikov, Statistical properties of a nonlinear string, Sov. Phys. Dokl. **11**, 57 (1966).

[12] B. Chirikov, F. Izrailev, and V. Tayursky, Numerical experiments on the statistical behaviour of dynamical systems with a few degrees of freedom, Comput. Phys. Commun. **5**, 11 (1973).

[13] B. V. Chirikov, A universal instability of many-dimensional oscillator systems, Phys. Rep. **52**, 263 (1979).

[14] R. MacKay and S. Aubry, Proof of existence of breathers for time-reversible or Hamiltonian networks of weakly coupled oscillators, Nonlinearity **7**, 1623 (1994).

[15] S. Flach and C. Willis, Discrete breathers, Phys. Rep. **295**, 181 (1998).

[16] D. K. Campbell, S. Flach, and Y. S. Kivshar, Localizing energy through nonlinearity and discreteness, Phys. Today **57**(1), 43 (2004).

[17] S. Flach and A. V. Gorbach, Discrete breathers—advances in theory and applications, Phys. Rep. **467**, 1 (2008).

[18] S. Flach, M. V. Ivanchenko, and O. I. Kanakov, q-Breathers and the Fermi-Pasta-Ulam Problem, Phys. Rev. Lett. **95**, 064102 (2005).

[19] S. Flach, M. V. Ivanchenko, and O. I. Kanakov, q-breathers in Fermi-Pasta-Ulam chains: Existence, localization, and stability, Phys. Rev. E **73**, 036618 (2006).

[20] G. P. Tsironis and S. Aubry, Slow Relaxation Phenomena Induced by Breathers in Nonlinear Lattices, Phys. Rev. Lett. **77**, 5225 (1996).

[21] K. O. Rasmussen, T. Cretegny, P. G. Kevrekidis, and N. Grønbech-Jensen, Statistical Mechanics of a Discrete Nonlinear System, Phys. Rev. Lett. **84**, 3740 (2000).

[22] M. Eleftheriou, S. Flach, and G. Tsironis, Breathers in one-dimensional nonlinear thermalized lattice with an energy gap, Physica D **186**, 20 (2003).

[23] M. Eleftheriou and S. Flach, Discrete breathers in thermal equilibrium: Distributions and energy gaps, Physica D **202**, 142 (2005).

[24] B. Gershgorin, Y. V. Lvov, and D. Cai, Renormalized Waves and Discrete Breathers in β-Fermi-Pasta-Ulam Chains, Phys. Rev. Lett. **95**, 264302 (2005).

[25] H. J. Matsuyama and T. Konishi, Multistage slow relaxation in a Hamiltonian system: The Fermi-Pasta-Ulam model, Phys. Rev. E **92**, 022917 (2015).

[26] Z. Zhang, C. Tang, and P. Tong, Dynamical thermalization of Frenkel-Kontorova model in the thermodynamic limit, Phys. Rev. E **93**, 022216 (2016).

[27] C. Bonatto, M. Feyereisen, S. Barland, M. Giudici, C. Masoller, J. R. R. Leite, and J. R. Tredicce, Deterministic Optical Rogue Waves, Phys. Rev. Lett. **107**, 053901 (2011).

[28] A. N. Ganshin, V. B. Efimov, G. V. Kolmakov, L. P. Mezhov-Deglin, and P. V. E. McClintock, Energy cascades and rogue waves in superfluid ^{4}He, J. Phys.: Conf. Ser. **150**, 032056 (2009).

[29] R. Höhmann, U. Kuhl, H.-J. Stöckmann, L. Kaplan, and E. J. Heller, Freak Waves in the Linear Regime: A Microwave Study, Phys. Rev. Lett. **104**, 093901 (2010).

[30] D. R. Solli, C. Ropers, P. Koonath, and B. Jalali, Optical rogue waves, Nature (London) **450**, 1054 (2007).

[31] H. S. Eisenberg, Y. Silberberg, R. Morandotti, A. R. Boyd, and J. S. Aitchison, Discrete Spatial Optical Solitons in Waveguide Arrays, Phys. Rev. Lett. **81**, 3383 (1998).

[32] F. Lederer, G. I. Stegeman, D. N. Christodoulides, G. Assanto, M. Segev, and Y. Silberberg, Discrete solitons in optics, Phys. Rep. **463**, 1 (2008).

[33] J. P. Bouchaud, Weak ergodicity breaking and aging in disordered systems, Journal de Physique I **2**, 1705 (1992).

[34] G. Bel and E. Barkai, Weak Ergodicity Breaking in the Continuous-Time Random Walk, Phys. Rev. Lett. **94**, 240602 (2005).

[35] G. Bel and E. Barkai, Random walk to a nonergodic equilibrium concept, Phys. Rev. E **73**, 016125 (2006).

[36] A. Rebenshtok and E. Barkai, Distribution of Time-Averaged Observables for Weak Ergodicity Breaking, Phys. Rev. Lett. **99**, 210601 (2007).

[37] A. Rebenshtok and E. Barkai, Weakly non-ergodic statistical physics, J. Stat. Phys. **133**, 565 (2008).

[38] C. Danieli, D. K. Campbell, and S. Flach, Intermittent many-body dynamics at equilibrium, Phys. Rev. E **95**, 060202(R) (2017).

[39] T. Mithun, Y. Kati, C. Danieli, and S. Flach, Weakly Nonergodic Dynamics in the Gross-Pitaevskii Lattice, Phys. Rev. Lett. **120**, 184101 (2018).

[40] T. Mithun, C. Danieli, Y. Kati, and S. Flach, Dynamical Glass and Ergodization Times in Classical Josephson Junction Chains, Phys. Rev. Lett. **122**, 054102 (2019).

[41] V. Arnold, *Mathematical Methods of Classical Mechanics* (Springer-Verlag, New York 1989), Vol. 60.

[42] S. Flach, M. Ivanchenko, O. Kanakov, and K. Mishagin, Periodic orbits, localization in normal mode space, and the Fermi-Pasta-Ulam problem, Am. J. Phys. **76**, 453 (2008).

[43] We obtained the prefactor A for Fig. 3 (LRN case) and Fig. 6 (SRN case) separately by computing the ratio $A \equiv T_E/\tau_q$ for one case of each figure. Specifically, for Fig. 3 $A \equiv T_E/\tau^+_{q,32} = 166$ is computed for mode $k = 32$ at $h = 0.1$; for Fig. 6 $A \equiv T_E/\tau^+_q = 132$ is computed for the weak-coupling regime at $\varepsilon = 0.1$ for $h = 5$.

[44] M. Ivanchenko, O. Kanakov, V. Shalfeev, and S. Flach, Discrete breathers in transient processes and thermal equilibrium, Physica D **198**, 120 (2004).

[45] R. Livi, M. Pettini, S. Ruffo, and A. Vulpiani, Chaotic behavior in nonlinear Hamiltonian systems and equilibrium statistical mechanics, J. Stat. Phys. **48**, 539 (1987).

[46] D. Escande, Stochasticity in classical hamiltonian systems: Universal aspects, Phys. Rep. **121**, 165 (1985).

[47] D. Escande, H. Kantz, R. Livi, and S. Ruffo, Self-consistent check of the validity of Gibbs calculus using dynamical variables, J. Stat. Phys. **76**, 605 (1994).

[48] Y. V. Lvov and M. Onorato, Double Scaling in the Relaxation Time in the β-Fermi-Pasta-Ulam-Tsingou Model, Phys. Rev. Lett. **120**, 144301 (2018).
[49] L. Pistone, M. Onorato, and S. Chibbaro, Thermalization in the discrete nonlinear Klein-Gordon chain in the wave-turbulence framework, Europhys. Lett. **121**, 44003 (2018).
[50] J. Laskar and P. Robutel, High order symplectic integrators for perturbed Hamiltonian systems, Celestial Mech. Dyn. Astron. **80**, 39 (2001).
[51] C. Skokos, D. O. Krimer, S. Komineas, and S. Flach, Delocalization of wave packets in disordered nonlinear chains, Phys. Rev. E **79**, 056211 (2009).
[52] A. Clauset, C. R. Shalizi, and M. E. J. Newman, Power-law distributions in empirical data, SIAM Rev. **51**, 661 (2009).
[53] R. P. Feynman, *Statistical Mechanics: A Set of Lectures*, Frontiers in Physics (Perseus Books, New York, 1972).
[54] S. Chakravarty and S. Kivelson, Photoinduced macroscopic quantum tunneling, Phys. Rev. B **32**, 76 (1985).
[55] M. Kac, G. Uhlenbeck, and P. Hemmer, On the van der Waals theory of the vapor-liquid equilibrium. I. Discussion of a one-dimensional model, J. Math. Phys. **4**, 216 (1963).
[56] W. Wang, J. H. P. Schulz, W. Deng, and E. Barkai, Renewal theory with fat tailed distributed sojourn times: Typical versus rare, Phys. Rev. E **98**, 042139 (2018).
[57] C. Skokos and E. Gerlach, Numerical integration of variational equations, Phys. Rev. E **82**, 036704 (2010).
[58] E. Gerlach and C. Skokos, Comparing the efficiency of numerical techniques for the integration of variational equations, Discr. Cont. Dyn. Sys. **2011**, 475 (2011).
[59] G. Enrico, S. Eggl, and C. Skokos, Efficient integration of the variational equations of multidimensional Hamiltonian systems: Application to the Fermi Pasta Ulam lattice, Int. J. Bifurcation Chaos **22**, 1250216 (2012).
[60] B. Senyange and C. Skokos, Computational efficiency of symplectic integration schemes: Application to multidimensional disordered Klein-Gordon lattices, Eur. Phys. J.: Spec. Top. **227**, 625 (2018).